Soil Dynamics and Earthquake Engineering 210 (2026) 110522

Contents lists available at ScienceDirect

Soil Dynamics and Earthquake Engineering

journal homepage: www.elsevier.com/locate/soildyn

Dynamic failure mechanisms of an urban sinkhole collapse revealed by dense near-field seismic observations

Tae-Kyung Hong [a,*], Byeongwoo Kim [a], Seongjun Park [a,b], Jeongin Lee [a], Junhyung Lee [a]

[a] Yonsei University, Department of Earth System Sciences, 50 Yonsei-ro, Seodaemun-gu Seoul 03722, South Korea

[b] Ocean Georesources Research Department, Korea Institute of Ocean Science and Technology, Busan 49111, South Korea

ARTICLE INFO

Keywords:
Sinkhole
Seismic monitoring
Urban hazards
Collapse dynamics
High-frequency signals
Ambient-noise cross-correlation

ABSTRACT

Sinkholes pose serious hazards to public safety and urban infrastructure, yet their dynamic failure processes remain poorly constrained due to the lack of direct subsurface observations. We investigate an urban sinkhole collapse that occurred in April 2025 in the southeastern suburbs of Seoul, South Korea, using dense near-field seismic observations acquired from a local seismic network. Detailed analyses of seismic waveforms, source characteristics, and spectral properties provide new insights into the dynamic failure mechanisms for sinkhole collapse. The seismic records reveal that the event comprised two successive major collapse phases separated by approximately 1.4 s, accompanied by prominent high-frequency impulsive signals. These high-frequency components are interpreted as small-scale brittle failures associated with cracking and fracturing within the collapsing ground mass. The inferred failure sequence involves an initial lateral expansion of an underground cavity, followed by vertical roof collapse and subsequent progressive brittle fracturing. Ambient-noise cross-correlation analyses further show clear traveltime perturbations and modifications of Green's functions in the frequency range of 0.5–4.0 Hz, indicating changes in near-surface elastic properties induced by the collapse. These observations demonstrate that dense near-field seismic monitoring provides a sensitive and non-invasive approach to resolving the dynamic evolution of sinkhole failure processes in urban environments. The results highlight the potential of urban seismic networks to improve the assessment of ground stability and support hazard mitigation strategies for sinkhole-related risks.

1. Introduction

Sinkhole formation and collapse represent a progressive geotechnical failure process governed by subsurface material degradation and stress redistribution, capable of causing severe damage to infrastructure and posing significant risks to public safety, particularly in densely populated urban areas. Sinkholes develop through a combination of gravitational deformation, internal erosion, and dissolution of subsurface materials, triggered by natural or anthropogenic factors, and often culminate in sudden ground-collapse events [1,2]. Sinkhole phenomena are commonly characterized by their dimensions, subsidence displacement, and deformation kinematics [3], and frequently result in the failure of buildings, roadways, and underground utilities [4–7]. Despite extensive observational and modeling efforts, the underlying mechanical processes governing sinkhole initiation and collapse remain insufficiently constrained.

In recent decades, anthropogenic sinkholes have become increasingly prevalent in urban regions due to intensive underground development, leakage from buried utilities, and excessive groundwater withdrawal. Early detection of sinkhole formation is therefore critical to minimize potential hazards and economic losses. However, despite extensive studies on sinkhole mechanisms and triggering processes [2,8], reliable real-time detection and monitoring techniques remain limited. A detailed understanding of the mechanical and physical processes operating during sinkhole evolution is essential for the development of effective monitoring and early-warning systems. In particular, mechanical signals generated during collapse may contain diagnostic information on subsurface failure processes and precursory deformation leading to sinkhole formation.

Sinkhole processes involve complex deformation of the surrounding medium and changes in subsurface mechanical properties associated with the creation and evolution of underground voids. Catastrophic collapses generate seismic waves that can be detected at local distances, suggesting that seismic monitoring offers a promising approach for identifying and characterizing sinkhole events. High-frequency surface waves are particularly sensitive to shallow subsurface anomalies, and multichannel surface-wave analysis has been successfully applied to

* Corresponding author.
E-mail address: tkhong@yonsei.ac.kr (T.-K. Hong).

https://doi.org/10.1016/j.soildyn.2026.110522
Received 15 January 2026; Received in revised form 1 July 2026; Accepted 1 July 2026
Available online 9 July 2026

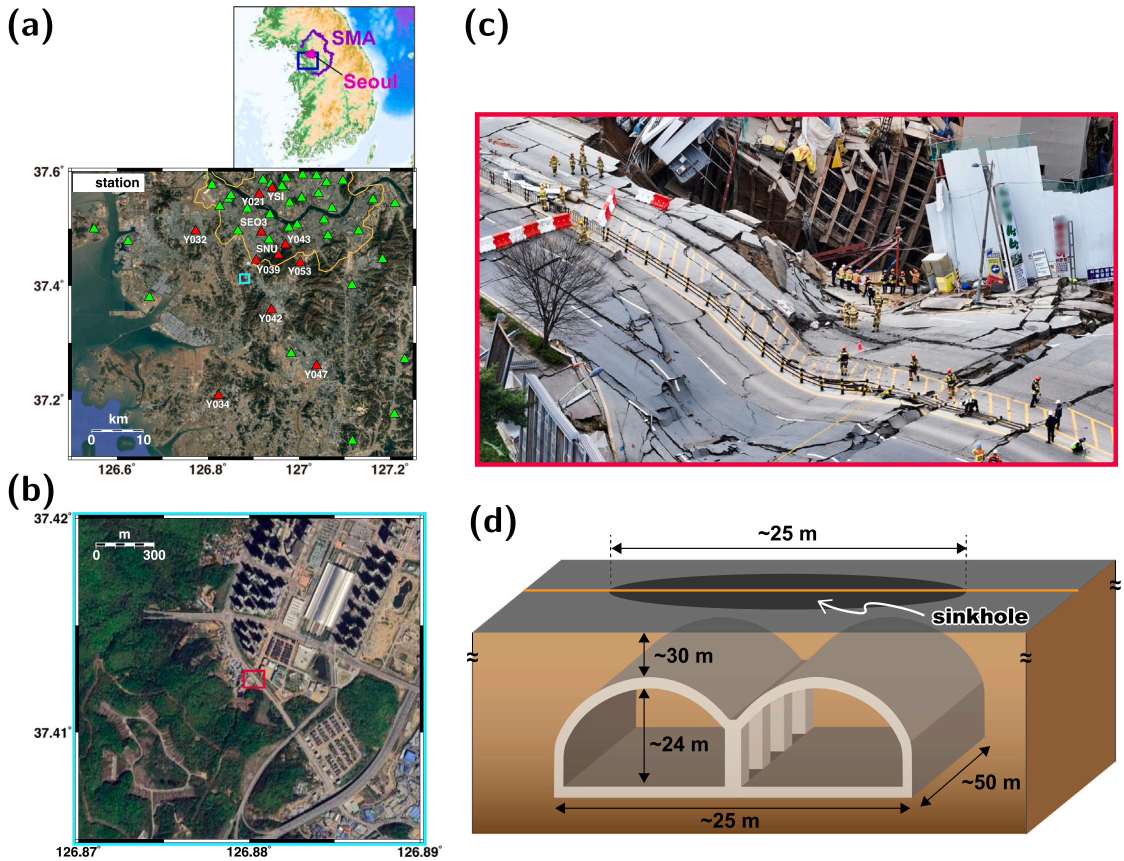

Fig. 1. (a) Map of the Seoul metropolitan area (SMA), Seoul, sinkhole event and seismic stations. The sinkhole event occurred in the southern outskirts of Seoul. Seismic stations near the sinkhole site are marked by triangles. Stations used for waveform inversion and wavetrain analyses are labeled by station name. The inset presents the location of the sinkhole site within the Korean Peninsula. (b) Enlarged map of the area surrounding the sinkhole. The boxed region indicates the location of the sinkhole site. (c) Photograph of the sinkhole site. The road surface is vertically displaced downward. (d) Schematic subsurface structure of sinkhole site. The sinkhole event occurred on a subway construction site. Satellite maps were retrieved from Google Maps.

detect underground voids and weak zones [9]. Moreover, analyses of local seismic waveforms allow inference of source mechanisms for non-earthquake events, providing physically meaningful constraints on subsurface collapse processes [10–12]. Seismic observations can therefore be used to infer changes in near-surface stiffness, damage accumulation, and failure mechanisms associated with sinkhole development. Nevertheless, urban seismic monitoring is often challenged by high levels of anthropogenic noise that obscure weak signals from small-scale collapses [13].

The Seoul metropolitan area provides a unique environment for investigating anthropogenic sinkhole processes (Fig. 1). A dense urban seismic network deployed in this region enables high-resolution monitoring of small seismic events, even under strong ambient noise conditions [14,15]. Unlike previous sinkhole studies that rely primarily on geotechnical surveys or post-collapse investigations, this study exploits near-field seismic waveforms and ambient-noise interferometry to directly resolve the collapse sequence, constrain the sinkhole failure mechanism, and quantify associated changes in near-surface mechanical properties. In this study, we analyze a sinkhole event that occurred in Seoul using data from this dense seismic network, demonstrating the potential of continuous urban seismic monitoring for sinkhole detection, ground stability assessment, and hazard mitigation.

2. Sinkhole event and data

Seoul is the capital city of South Korea. As of 2023, the population of the Seoul metropolitan area exceeded 26 million. A catastrophic sinkhole collapse occurred in southern suburban Seoul on April 11, 2025 (Fig. 1). The sinkhole event occurred in a subway (Shinansan Line) tunnel construction site. A six-lane road above a subway tunnel under construction collapsed in a U-shape, producing a sinkhole with a diameter of ~25 m (Fig. 1(c),(d)). The subway tunnel is located ~30 m below the surface. The two-lane subway tunnel has a dimension of ~24 m height and ~25 width. The length of damaged tunnel is ~50 m.

The subway tunnel collapse occurred in a mechanically weak subsurface environment dominated by weathered soil and rock. The medium above the tunnel has high water content, which leaks during tunnel construction. The high water produces weight above the tunnel, making vertical pressure on the tunnel. Anomalous increases in deformation, accompanied by progressive crown settlement, tunnel cross-sectional distortion, and partial failure of internal support structures occurred prior to the sinkhole. The event is interpreted as the result of combined weak ground conditions and progressive instability during tunnel excavation.

A dense seismic network is available in the Seoul metropolitan area (Figs. 1(a) and 2(a)). The seismic network in the Seoul metropolitan area comprises 55 permanent stations and 60 temporally deployed stations, all equipped with broadband seismic sensors. There are 79 stations in the region within a 50 km radius of the sinkhole site. The interstation distances range from 0.9 to 23.1 km. We collect seismic records from the stations. The surface collapse of the sinkhole was recorded by seismometers at local distances (Fig. 3).

We additionally collect seismic records from collocated surface and borehole seismometers at depths of 0 m, 300 m, and 600 m to examine waveform variations with sensor depth (Fig. 3(e)). The collocated seismometers are installed in the Earth Observatory, Yonsei University.

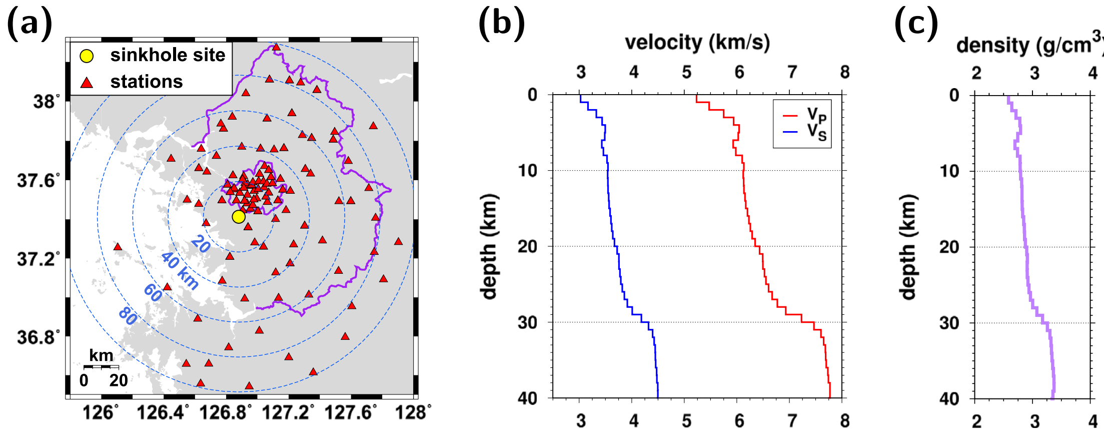

Fig. 2. (a) Map of seismic stations in the Seoul metropolitan area and neighboring regions. The sinkhole site is marked by a circle. (b) Reference 1-D *P*- and *S*-wave velocity models for the Seoul metropolitan area, and (c) the corresponding reference density model.

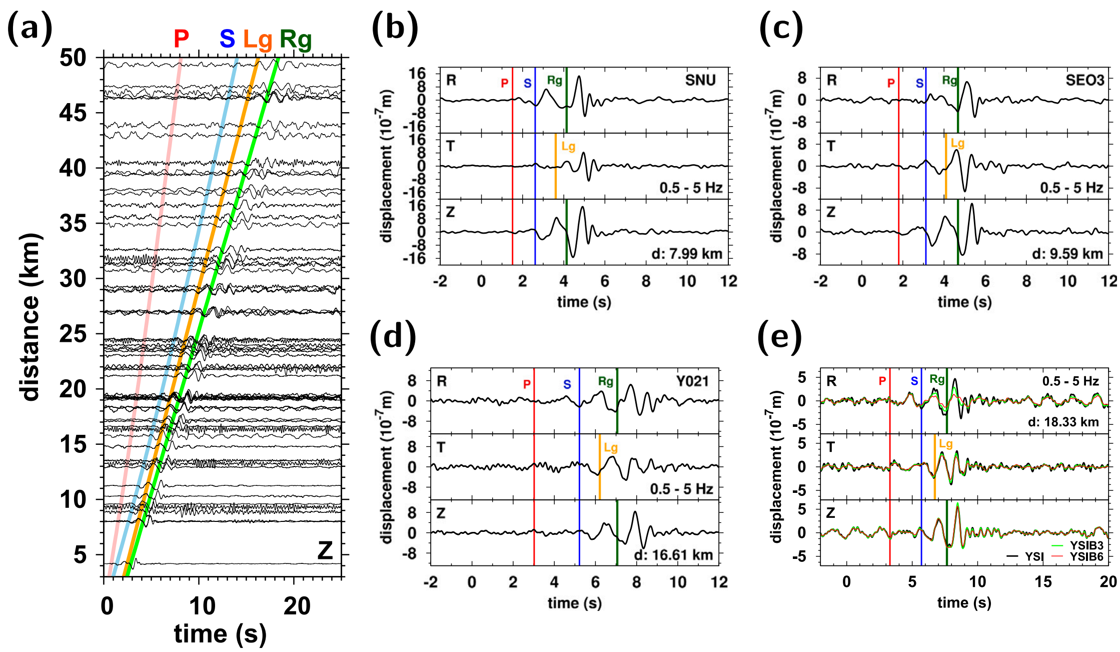

Fig. 3. (a) Vertical seismic waveform records for the sinkhole event. The traveltime curves of major phases (*P, S, Lg, Rg*) are presented (solid lines). Three-component seismic waveform records at stations (b) SNU, (c) SEO3, (d) Y021, and (e) collocated seismometers (YSI, YSI3, YSI6). The locations of stations are marked in the map (Fig. 1(a)). The seismic waveforms are bandpass-filtered between 0.5 and 5 Hz. The distances (*d*) are presented. The theoretical arrival times of major phases are indicated (vertical solid lines). The surface-wave amplitudes in the collocated seismometers decrease with increasing sensor depth.

We also compile 1-D *S*-wave velocity (V_S) models for 72 stations in the Seoul metropolitan area derived from receiver function analyses [16]. These models are used to construct local reference seismic velocity models (Fig. 2; Fig. S1 in the Supplementary Materials).

3. Methods

We conduct a long-period waveform inversion to find a source mechanism solution (moment tensor solution) for the sinkhole. The seismic source can be decomposed into three sets of moment tensors, representing a double couple, isotropic, and compensated linear vector dipole (CLVD) components [17,18]. We determine the full moment tensor solution using a parabolic source time function for the observed waveforms [18,19]. The parabolic source time function is useful for inversion of non-natural seismic events [20]. The parabolic source time function, $s(t)$, is given by [18]

$$s(t) = \frac{1}{2T_0}\begin{cases} 0, & t \le 0 \\ \frac{1}{2(t/T_0)^2}, & 0 < t \le T_0 \\ -\frac{1}{2(t/T_0)^2} + 2(t/T_0) - 1, & T_0 < t \le 3T_0 \\ \frac{1}{2(t/T_0)^2} - 4(t/T_0) + 8, & 3T_0 < t \le 4T_0 \\ 0, & t > 4T_0 \end{cases} \tag{1}$$

where t is the time in seconds, and T_0 is a constant that controls the source duration time. The synthetic waveforms are calculated using a normal mode summation method based on a reference 1-D velocity model [18,21,22]. We apply the representative 1-D velocity model for the Seoul metropolitan area from a receiver function analysis for the reference velocity model [16].

The sinkhole event may be composed of a series of subevents. We identify major subevents from the observed wavetrains, determining their source mechanisms individually. The full sinkhole event is represented by combining the individual source mechanisms. We verify the full sinkhole source mechanism by comparing the synthetic wavetrains with the observed wavetrains. The synthetic wavetrains are additionally calculated using the reflectivity method, which is effectively applicable to layered media [12,23–25]. The reflectivity method effectively considers the reflected phases and trapped waves, as well as direct waves, which are well observed at local distances for near-surface sources.

We extract the Green's function of seismic waves traveling between two stations using an ambient-noise cross-correlation technique [21,22,26,27]. Waveform cross-correlation function is given by [26,27]

$$C_{ij}(t) = \frac{\int u_i(t+\tau)u_j(\tau)d\tau}{\sqrt{\int \left[u_i(t+\tau)\right]^2 d\tau}\sqrt{\int \left[u_j(\tau)\right]^2 d\tau}}, \tag{2}$$

where t is the delay time, C_{ij} is the waveform cross-correlation function between stations i and j, and $u_i(\tau)$ and $u_j(\tau)$ are the waveform records at time τ for stations i and j. The Green's functions are obtained by stacking of noise cross-correlation functions. The stability in the Green's function increases with an increasing number of ambient-noise cross-correlation functions. We empirically determine the number of stacking ambient-noise cross-correlation functions [21,22]. The number of stacked ambient-noise cross-correlation functions increases with frequency. The Green's functions are compared to examine temporal changes in medium properties.

4. Analysis

The sinkhole event was captured by the dense seismic network in the Seoul metropolitan area. Seismic stations located near the sinkhole site are used for waveform, spectral, source-inversion, and ambient-noise analyses. These primary stations include SNU, Y021, SEO3, YSI, YSI3, YSI6, Y034, Y039, Y042, and Y053 (Fig. 1(a)). The raw seismic records are obtained in three components (NS, EW, and vertical components). The horizontal components are then rotated from the NS-EW coordinate system into radial and tangential components using a standard coordinate rotation.

For the examination of waveform features, we analyze seismic records from all stations in the Seoul metropolitan area (Fig. 2(a)). The seismic waveforms are bandpass-filtered between 0.5 and 5.0 Hz (Fig. 3). We distinguish individual subevents based on waveform characteristics prior to conducting moment tensor inversions. We examine the wavetrains of the sinkhole event. The *Rg* wavelets, along with their phase velocities and spectral contents, provide important information about the number of individual subevents. Moment tensor inversion is then applied to each subevent. We finally verify the identified subevents by comparing the combined synthetic waveforms with the observed waveforms.

The source mechanism may provide insight into the sinkhole process. We determine the source mechanism and event magnitude from a long-period waveform inversion. We constrain the source mechanism of the sinkhole event using seismic records from seven local stations: SEO3, SNU, Y034, Y039, Y042, Y043, and Y053 in Fig. 1(a). The source time function $s(t)$ for moment tensor inversion is represented by a parabolic function. The source duration time T_0 is determined by searching over a range of duration constants to achieve the optimal fit between the observed and synthetic waveforms.

Spatially heterogeneous distributions of noise-inducing sources lead to anisotropic ambient seismic wavefields, causing retrieved surface waves to exhibit preferential propagation along specific directions [28,29]. Anthropogenic activity in urban areas commonly generates more spatially uniform and isotropic high-frequency surface waves [13]. Such conditions facilitate the stable reconstruction of high-frequency Green's functions from ambient-noise cross correlations in urban regions.

We perform the interstation ambient-noise cross-correlation analysis using continuous seismic waveform records. All waveforms are corrected for the instrument response and band-pass filtered for a frequency range between 0.01 and 10 Hz. Running-absolute-mean normalization and spectral whitening are applied to the waveforms to suppress transient signals, minimizing the influence of frequency content on the analysis. The crosscorrelation functions are computed for consecutive 2-hour-long time windows. Here, time windows including data gaps are excluded from the analysis. The calculated cross-correlation functions are then stacked over the targeted time period, yielding the representative Green's function for that period.

Ambient noise varies with the time of day, day of the week, season, and long-term environmental conditions [29–32]. Thus, the optimal stacking duration should be determined empirically considering the characteristics of local ambient noise field (Fig. S10 in the Supplementary Materials). The required stacking duration is selected to achieve stable cross-correlation functions under the prevailing noise conditions. High frequency noise is difficult to be stabilized from stacking process (Fig. S11 in the Supplementary Materials). Thus, the high frequency data require stacking over more days (see the Supplementary Materials).

The stacked ambient-noise cross-correlation functions yield empirical Green's functions that correspond to wavetrains composed of wavelets traveling between stations. The amplitudes of wavelets are strongly affected non-ideal factors such as the distribution of ambient-noise sources, temporal variations in source strength, and waveform preprocessing procedures. Thus, these waveforms are regarded as reliable primarily for their phase information including traveltimes, dispersion characteristics, and relative waveform shapes. The waveforms are presented as normalized wavetrains without indication of absolute amplitudes.

The reference 1-D shear-wave velocity (V_S) model is constructed by averaging the collected 1-D *S*-wave velocity models for 72 stations in the Seoul metropolitan area (Fig. 2). The reference *P*-wave velocity (V_P) model is then determined using the reported average crustal V_P/V_S ratio of 1.73 [16]. In addition, the reference density model is derived from the reference velocity model using an empirical relationship [16,33]. These reference 1-D V_P and V_S models are used to calculate Green's functions and theoretical traveltime curves for the long-period waveform inversion and theoretical traveltime calculations.

5. Seismic waveform features

The observed wavetrains are mainly composed of major local phases at distances of <100 km (Fig. 3; Fig. S2 in the Supplementary Materials). We observe apparent *P* waves that are followed by *S*, crustally guided shear waves (*Lg*), and fundamental-model Rayleigh waves (*Rg*). The wavetrains suggest efficient transmission of seismic phases across the Seoul metropolitan area.

The *P* waves are strong in the radial component at near distances, while weak in the vertical component. The dominant *P* energy in the radial component agrees with the effective lateral energy propagation from shallow-focus events at short distances (Fig. 3). The *P* polarization directions are subparallel to the radial directions, presenting apparent *P* energy in the radial components (Fig. 3; Fig. S3 in the Supplementary Materials). Also, the *P* energy is observed in various azimuths, suggesting azimuthally isotropic source excitation.

The surface waves (*Lg*, *Rg*) are strong events at distances less than 5 km. The *Lg* phase is clear in the tangential component. The *Lg* phase arrives earlier than *Rg*. The apparent phase velocity of *Lg* is 3.32 km/s, and that of *Rg* is 2.95 km/s. Thus, the *Rg* and*Lg* waves are not fully separated at local distances, presenting mixed wavetrains. The Rayleigh waves present elliptical retrograde particle motions in the vertical–radial plane (Fig. 4; Fig. S4 in the Supplementary Materials).

The phase arrivals reasonably match the theoretical traveltime curves based on the reference 1-D velocity model (Fig. 3). Note that the *P* and *S* wave velocities in the reference velocity model are 5.67 km/s and 3.28 km/s, respectively. The traveltime agreement confirms the

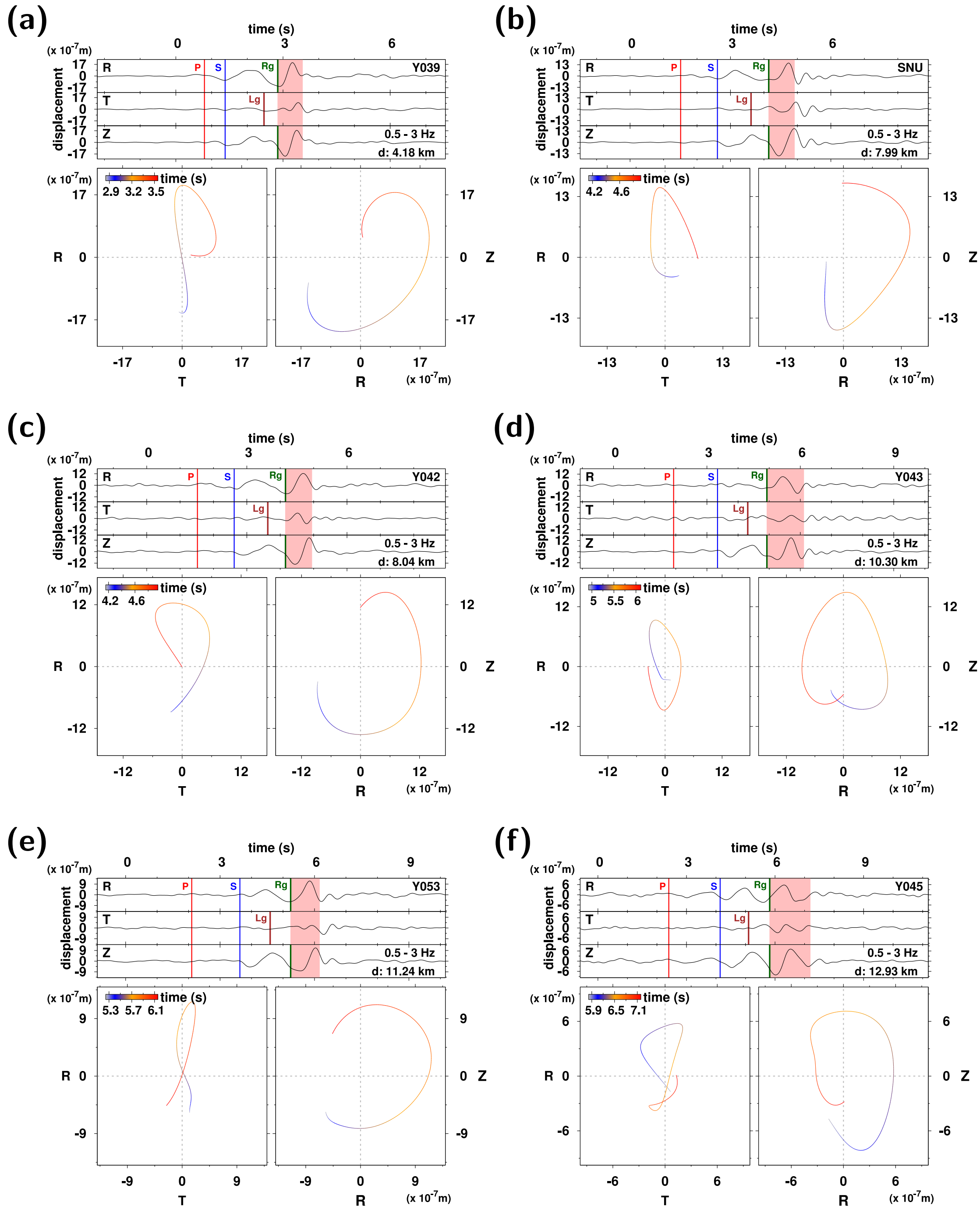

Fig. 4. Three-component (R, T, Z) wavetrains and particle motions of Rayleigh waves (shaded parts in wavetrains) in frequencies of 0.5–3.0 Hz at stations (a) Y039, (b) SNU, (c) Y042, (d) Y043, (e) Y053, and (f) Y045. The locations of stations are marked in Fig. 1(a). The distances (*d*) are indicated. The Rayleigh waves are polarized in the radial (R) direction, presenting retrograde elliptical particle motions on the R-Z plane.

origin time and location of the sinkhole event. The *P* energy is relatively strong in the radial component at short distances, <10 km. By contrast, the *P* is relatively weak in the vertical and tangential components. At larger distances (>10 km), the *P* energy in the radial component is low in amplitude due to the influence of heterogeneous media near the surface during its lateral propagation.

We determine the energy polarization of surface waves (Fig. 4). The seismic-wave energy dominantly appears in the radial component relative to the tangential component due to the preferential development of *Rg*. The *Rg* waves are strong in both vertical and radial components (Fig. 4). The *Rg* phase presents the characteristic retrograde particle motions on the vertical plane (Fig. 4). The decreasing phase amplitudes with increasing sensor depth in the radial and vertical components of the co-located stations verify the *Rg* phase (Fig. 3(e)). We observe *Lg* waves in the tangential component, with site-to-site variations (Fig. 3). The site-dependent *Lg* development may be associated with local crustal heterogeneities. The strong *Rg* and weak *Lg* suggest azimuthally-isotropic energy radiation with weak *SH* energy.

The waveforms of major phases at similar distances are similar, varying little with azimuth (Fig. 3). The observation suggests nearly azimuthally homogeneous energy radiation from the source, implying source activation of a minor double-couple component and major non-double-couple (i.e., compensated linear vector dipole (CLVD) or isotropic) component. The weak double-couple component suggests

Soil Dynamics and Earthquake Engineering 210 (2026) 110522

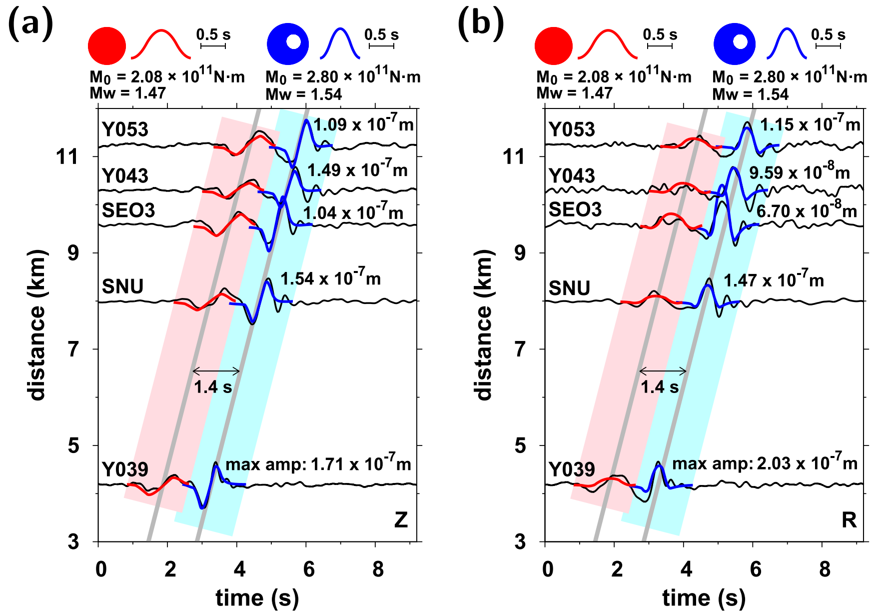

Fig. 5. Long-period waveform inversions for two major events. The comparison between synthetic and observed waveforms in (a) vertical (Z) and (b) radial (R) components. The locations of stations are marked in Fig. 1(a). The focal mechanism solutions are presented with seismic moments and moment magnitudes. The parabolic source time functions for the two major events are presented separately. The synthetic waveforms match well with the observed waveforms. The constant time lapse (1.4 s) between two *Rg* wavelets supports the occurrence of two events. The second major event occurs successively after the first event.

that the source may be hardly related to shear faulting (i.e, natural earthquake). The azimuthally homogeneous waveforms and strong surface waves may support effective vertical shallow mass movement along with azimuthally homogeneous energy radiation, which may be expected during the sinkhole event.

6. Multiple major events

We analyze the waveforms at three co-located sensors (YSI, YSI3, YSI6) with vertical separation located 18.33 km from the sinkhole (Fig. 1(a)). The arrival times of body waves are synchronized among the seismometers (Fig. 3(e)). However, we find characteristic waveform changes among the sensors at different depths (Fig. 3). The amplitude of surface waves in the radial component appears to decrease with increasing station depth. By contrast, the surface-wave amplitude changes are minimal in the vertical component. The effective amplitude change in the radial component suggests that the waveforms are composed of Rayleigh wavetrains.

We observe two consecutive *Rg* wavelets with similar apparent phase velocities, maintaining a nearly constant time separation of approximately 1.4 s across stations (Fig. 5). These two *Rg* phases exhibit different spectral characteristics (Fig. 6). The later *Rg* presents relatively high frequency content, while the earlier *Rg* phase displays relatively low frequency content. This feature indicates that these *Rg* wavelets are not part of a single dispersive wave packet but are more likely generated by two successive source processes. The long-duration nondispersive *Rg* wavelets may be interpreted as a set of successive multiple events at the sinkhole site. This observation suggests that such a feature can occur when a series of single events occurs in the same source location. We thus invert the two wavelets independently.

7. Source mechanism inversion

The two *Rg* wavelets with the same phase velocities suggest the successive occurrence of two different events during the sinkhole (Fig. 5). We determine the source mechanisms of two events. The waveform inversions are conducted for the two events independently considering the frequency contents of wavelets. We first conduct the waveform inversion for the later major event (the larger event). We use a parabolic source time function with a duration constant (T_0) of 0.2 s. The seismic moment tensor for the later event is given as (Fig. 5)

$$\mathbf{M} = M_0 \times \begin{pmatrix} 0.863 & -0.108 & -0.230 \\ -0.108 & 0.645 & -0.560 \\ -0.230 & -0.560 & -0.284 \end{pmatrix}, \quad (3)$$

where the seismic moment is $M_0 = 2.80 \times 10^{11}$ N m and the magnitude is M_W 1.54. The synthetic waveforms match the observed waveforms reasonably well. The event origin time for the later event is determined to be 06:10:57.9 on April 11, 2025 (UTC). The source mechanism suggests lateral expansion with vertical compression (Fig. S5 in the Supplementary Materials).

We then find the source mechanism parameters for the earlier major event (the smaller event). We apply a parabolic source time function with a duration constant (T_0) of 0.3 s (Fig. 5). The seismic moment tensor for the earlier waveforms is given by

$$\mathbf{M} = M_0 \times \begin{pmatrix} 0.907 & -0.087 & -0.163 \\ -0.087 & 0.922 & -0.276 \\ -0.163 & -0.276 & 0.326 \end{pmatrix}. \quad (4)$$

Here the seismic moment is $M_0 = 2.08 \times 10^{11}$ N m, and the magnitude is M_W 1.47. The event presents dominant volumetric expansion. The two events present dominant lateral expansion, with a possible difference in vertical deformation. The two events are separated by ~1.4 s, which is clearly observed in the wavetrains among the stations (Fig. 5). Additionally, the two events present a characteristic difference in frequency content. The synthetic waveforms from the two source mechanisms match reasonably with the observed individual waveforms. The observed T_0 values (0.3 s for the earlier event and 0.2 s for the later event) are consistent with the durations of the observed *Rg* wavelets.

We first calculate the synthetic waveforms for the source mechanisms of the two major events using the normal-mode summation method. We then combine the wavetrains to produce the full wavetrains for the sinkhole event (Fig. 7). The combined synthetics reasonably reproduce the observed wavetrains, and the waveform comparison verifies the successive occurrence of the two events and their source mechanisms. These observations suggest two successive collapse processes. We crosscheck the wavetrains using the reflectivity method,

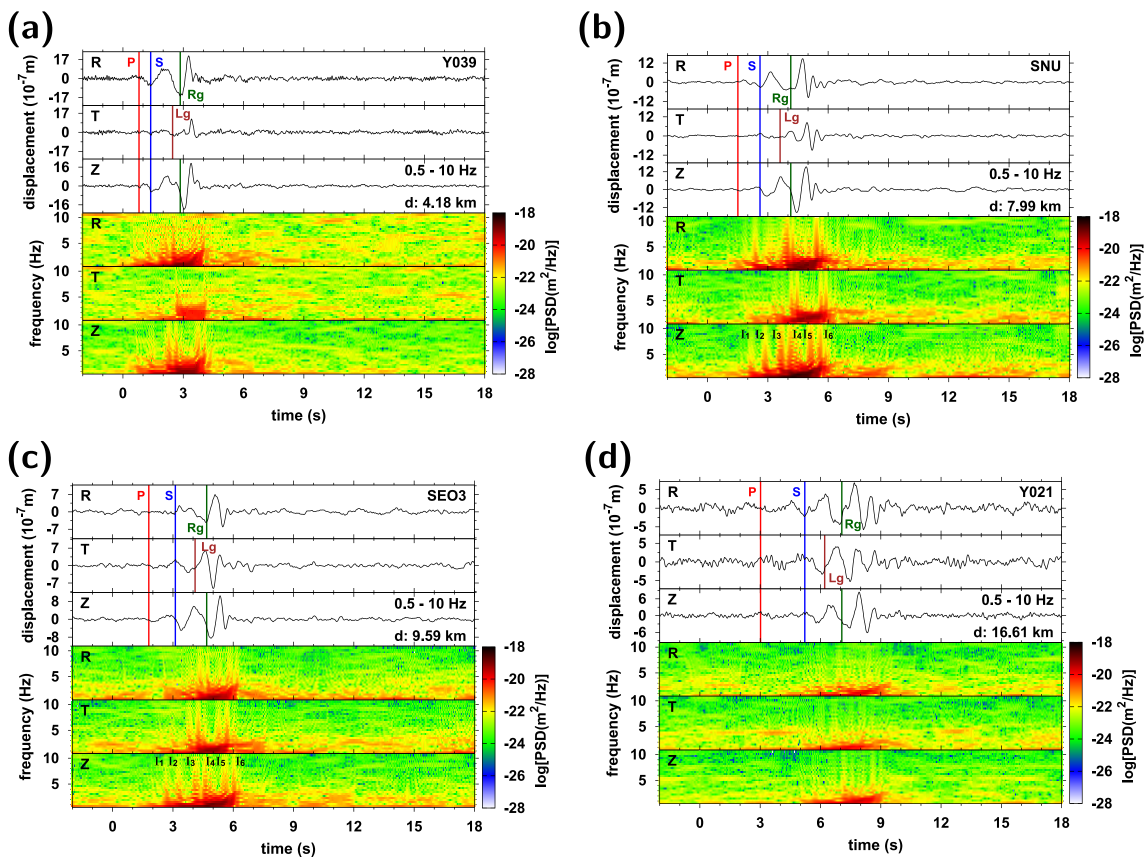

Fig. 6. Three-component spectrograms of wavetrains at stations (a) Y039, (b) SNU, (c) SEO3, and (d) Y021. The distances (d) are indicated. The arrival times of major phases are marked (vertical solid lines). Impulsive signals (I_1, I_2, $\cdots$, I_n) are observed, overlapping with major phases in the spectrograms.

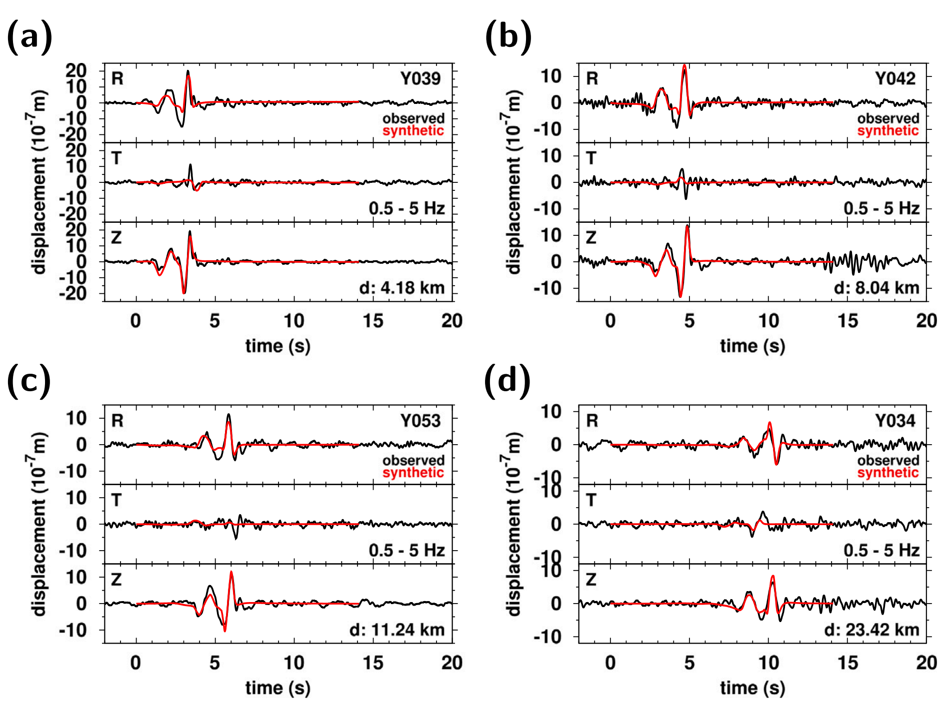

Fig. 7. Modeling of seismic waveforms based on a normal-mode summation method for two successive events at stations (a) Y039, (b) Y042, (c) YO53, and (d) Y034. The distances (d) are indicated. The waveforms are bandpass-filtered between 0.5–5.0 Hz. The synthetic waveforms agree well with the observed waveforms.

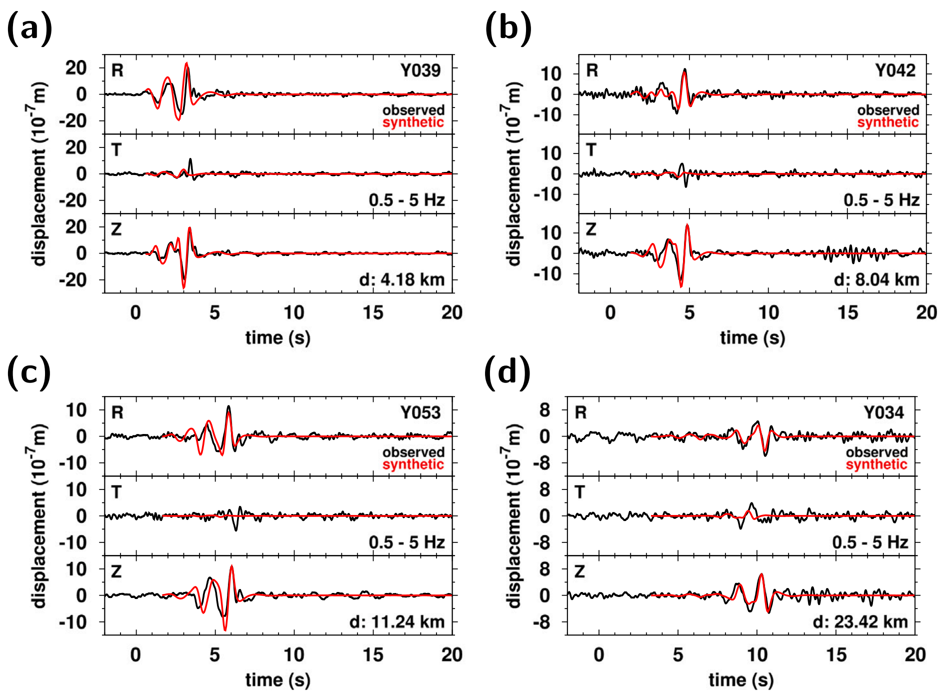

Fig. 8. Modeling of seismic waveforms based on a reflectivity method for two successive events at stations (a) Y039, (b) Y042, (c) YO53, and (d) Y034. The distances (d) are indicated. The waveforms are bandpass-filtered between 0.5–5.0 Hz. The synthetic waveforms generally agree with the observed waveforms.

which is effective for waveform synthesis in a layered medium (Fig. 8). The synthetic wavetrains match well with the observed wavetrains, supporting the phase identification.

We further examine the possible representation of the wavetrains using a single source with a long-duration source-time function that combines the major events. We search for the best-fit source duration time to produce the best-fit wavetrains. The best-fit time interval between the two major events is 1.3 s, which is close to 1.4 s, the time interval inferred from the long-period waveform inversions. We find that the vertical and radial synthetic waveforms reasonably match the observed waveforms. The waveform simulation based on a single event with a long-duration source time function produces similar results to those based on two separate independent sources. This observation suggests that the two major events may constitute a successive process of a single complex sinkhole event.

8. Stability tests of moment tensor inversions

We examine the stability of long-period waveform inversion results with respect to station selection. We repeatedly perform moment tensor inversions while excluding one station at a time from the full station set, keeping the source location, filtering band, time window, source-time function, and reference velocity model fixed. The results consistently reproduce the main source characteristics. The earlier event is characterized by vertical compression accompanied by lateral expansion, whereas the later major event is characterized by volumetric expansion. These features suggest that the sinkhole formed through a series of consecutive events.

We also examine the sensitivity of the inversion results to the adopted 1-D velocity models (Fig. 9). The inversions are repeated using the global average 1-D velocity model ak135 [34]. We further test perturbed models with velocity variations of ±3 % relative to the reference model (Fig. 9(a)–(c)). For the larger event (the later major event), the global average and perturbed velocity models consistently reproduce the dominant source characteristics, with only minor variations in component amplitudes (Fig. 9(e)–(g)). All inversion results indicate vertical compression accompanied by lateral expansion and volumetric expansion.

We further assess the stability of the inversion results by excluding individual stations (SEO3, Y042, Y043, and Y053). The inversion results remain consistent for all cases (Fig. 9(h)–(k)). Finally, we conduct the same tests for the smaller event (the earlier major event). All results consistently present volumetric expansion. These observations support the robustness of the main source interpretation.

9. Minor associate events

The spectral contents may reflect the source physics. We infer additional source properties from the spectral contents of the waveforms at stations in short distances (<20 km) (Fig. 6). The constitutive energy is dominant at frequencies of <5 Hz, and it is similar among the three components. The surface waves are strong in frequencies at <2 Hz, and mild in frequencies at 2–5 Hz. The spectra of the surface waves present a dispersive feature (Fig. 6).

We find a series of impulsive energy at 3–15 Hz that appears in the surface-wave wavetrains at both permanent and temporally-deployed stations (I_1, I_2, ⋯, I_n in Fig. 6). The impulsive energy is particularly strong at short distances (<20 km). The impulsive energy is strong up to 15 Hz, which is higher than the spectral contents of the apparent seismic phases of the sinkhole event. We observe impulsive energy continuing even after the surface waves. Furthermore, we consistently observe impulsive energy within common seismic phases at different stations, supporting the conclusion that they share the same origin.

The impulsive energy is apparent in the surface-wave wavetrains, while it is weak in the body-wave phases. The inconsistent appearance of impulsive energy among three components (R, T, Z) and its consistent appearance in common phases at different stations suggest that the energy is delivered with the seismic phases. The impulsive energy may represent successive minor collapses (such as mass drops) that occur during and after the catastrophic main collapse.

10. Sinkhole formation process

The waveform and spectral analyses suggest that the sinkhole event is comprised of two successive major collapses and minor associated

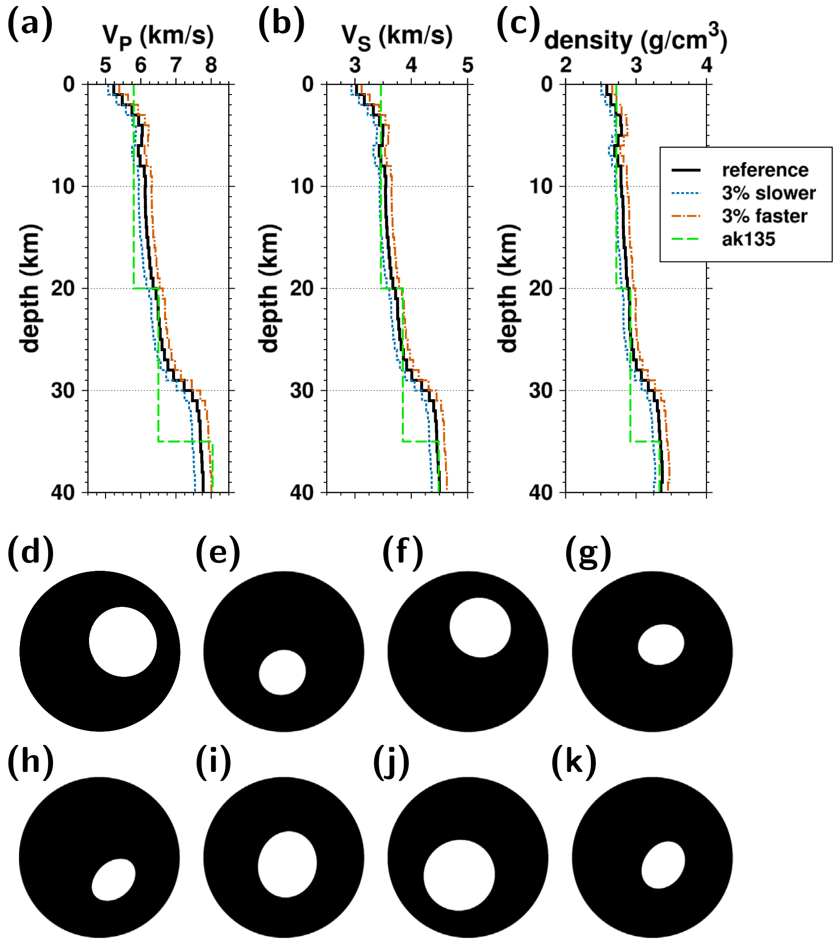

Fig. 9. Collections of (a) *P*-wave velocity (V_P) models, (b) *S*-wave velocity (V_S) models, and (c) density models. Sensitivity tests of long-period waveform inversion for seismic velocity models using (d) the reference velocity model, (e) the global average 1-D velocity model ak135, (f) a 3% faster model, and (g) a 3% slower model relative to the reference velocity model. Leave-one-station-out tests excluding stations (h) SEO3, (i) Y042, (j) Y043, and (k) Y053. All tests yield consistent source mechanisms, supporting the stability of the inversion results.

events. The observed source mechanisms provide information on the physical mass movement during the sinkhole event. The two linked successive major collapses enable us to understand the sinkhole process. The source mechanisms suggest two stages of collapses: an initial lateral expansion (first collapse stage) followed by a subsequent vertical collapse with lateral expansion (second collapse stage). This observation suggests that initial lateral tunnel expansion induced successive vertical collapse and additional lateral expansion (Fig. 10).

The source mechanism indicates sudden mass collapse with successive or coincident lateral mass movement. The source mechanism solutions and wavetrains suggest lateral expansion sustained for 1.3 s. Eventually, the surface load (e.g., cemented cover) collapsed into the void space beneath the surface. The collapse produces vertical compression and further lateral expansion. The proposed source mechanism is consistent with the reported internal collapse characteristics and the resulting surface deformation. The inferred source process suggests that the collapse generated vertical surface subsidence accompanied by progressive outward failure around the excavation zone (Fig. 10). Also, the tunnel collapse was associated with outward structural deformation and related mass movement.

The spectral contents suggest the constituent mechanical activity during the sinkhole process. The low-frequency energy suggests the entire duration of the sinkhole process. Multiple impulsive energy (spectral streaks) may indicate a series of small-scale subsurface collapses or fracturing that may be associated with the main collapse. In particular, the observed major and minor events may be associated with brittle medium deformation (collapse) and suffosion with downward mass movement in subsurface voids [2]. Thus, the observed sinkhole wavetrains may be the combined result of vertical surface-layer collapse and associated subsurface brittle medium deformation.

It is noteworthy that we observe mild energy in the tangential components. The tangential-component energy suggests laterally inhomogeneous energy radiation that may be associated with vertically tilted mass movement and laterally anisotropic energy excitation. Additionally, laterally heterogeneous media may also contribute to the development of the tangential-component energy.

11. Near-surface damage and velocity perturbations

Sinkholes may cause medium perturbations. The strength of medium perturbations may depend on the size of the sinkhole, which may be reflected in the event magnitude. Green's functions are sensitive to variations in medium properties. We estimate seismic traveltime and phase variations in Green's functions retrieved from ambient-noise cross-correlation functions for paths crossing the sinkhole site. High-frequency Rayleigh waves are particularly sensitive to changes in shallow subsurface structures (Figs. S6 and S7 in the Supplementary Materials).

Stable estimation of changes in medium properties requires appropriate selection of the frequency band based on wavelength and depth sensitivity. We analyze ambient-noise cross-correlation functions in the 0.5–1.0 Hz, 1.0–2.0 Hz, and 2.0–4.0 Hz frequency bands (Fig.

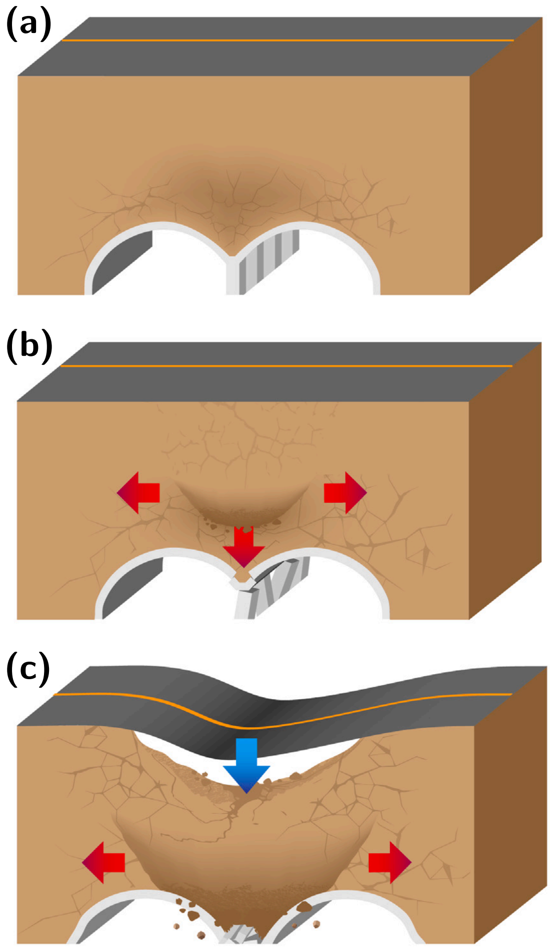

Fig. 10. Schematic model of sinkhole sequence: (a) crack and hole formation before the sinkhole event, (b) the internal-medium collapse for 1.4 s (first collapse stage), and (c) subsequent surface collapse (second collapse stage) and sinkhole formation. The first procedure excites seismic waves for a volumetric expansion source. The second procedure forms a vertical compression source with lateral expansion.

11). Stable Green's functions are retrieved from the stacked ambient-noise cross-correlation functions (Figs. S8 and S9 in the Supplementary Materials).

We examine temporal variations in the daily Green's functions (Fig. 12). Daily stacking is applied to the 0.5–1.0 Hz frequency band, while 7-day stacking is employed for the 1.0–2.0 Hz and 2.0–4.0 Hz frequency bands (Figs. S12 and S13 in the Supplementary Materials). Stable Green's functions are observed in the 0.5–1.0 Hz frequency band along all paths in the NE-SW and NW-SE directions. Similar Green's functions are identified for paths with comparable orientations, including Y039-Y034 and SEO3-Y034 along the NE-SW direction, and Y032-Y042 and Y032-Y047 along the NW-SE direction.

The daily Green's functions exhibit stable phase velocities, consistent wavelet shapes, and nearly constant travel times over most of the observation period before the sinkhole event (Fig. 12). Noticeable abrupt waveform distortions and travel-time perturbations are consistently observed across all analyzed frequency bands around the day of the sinkhole event. These variations are particularly pronounced at higher frequencies, reflecting the greater sensitivity of high-frequency surface waves to shallow subsurface structural changes. These observations suggest that temporal changes in the Green's functions can be evaluated using different empirical threshold levels.

Changes in waveform, wavelet composition, and phase are interpreted as temporal variations in the Green's functions. We observe apparent changes in Green's functions over the sinkhole event day (A, A', B, B', C, and C' in Fig. 12). The highlighted portions of the Green's functions exhibit pronounced temporal changes during the days surrounding the sinkhole event. The observations suggest that the sinkhole incorporates noticeable changes in medium properties.

The Green's functions in the 1.0–2.0 Hz and 2.0–4.0 Hz frequency bands are weakly reconstructed from 7-day ambient-noise cross correlations. We find mild changes in the Green's functions over the sinkhole event day in 1.0–2.0 Hz and 2.0–4.0 Hz (Figs. S12 and S13 in the Supplementary Materials). The observed features suggest that ambient-noise cross-correlation functions can be used to detect changes in medium properties caused by sinkholes.

12. Discussion and conclusions

The seismic analysis of the 11 April 2025 sinkhole event in the southern suburbs of Seoul provides new insights into the dynamic mechanical processes governing anthropogenic sinkhole formation in urban environments. The dense near-field seismic network enabled high-fidelity resolution of waveform characteristics and source mechanisms, allowing the temporal evolution and dynamic behavior of the collapse sequence to be examined in unprecedented detail.

Seismic waveform and spectral analyses indicate that the sinkhole collapse consisted of two distinct sub-events separated by approximately 1.4 s. The first sub-event is interpreted as the lateral expansion of a pre-existing underground cavity, likely driven by tunnel deformation or progressive void enlargement. The second sub-event represents vertical roof collapse, reflecting the ultimate gravitational failure of the overlying ground materials. This two-stage collapse sequence suggests that sinkhole formation is controlled by progressive subsurface weakening and stress redistribution, followed by abrupt structural failure. Such behavior is consistent with previously proposed progressive sinkhole development models, in which gradual cavity growth precedes catastrophic collapse [2,8].

High-frequency impulsive seismic signals accompanying the two major collapse phases are interpreted as small-scale brittle failures associated with cracking and fracturing of the surrounding materials. These signals likely reflect localized stress concentrations and damage accumulation during both cavity expansion and roof collapse. The occurrence of multiple minor seismic bursts indicates that sinkhole collapse is not an instantaneous process but rather a complex failure sequence involving both large-scale structural collapse and distributed brittle damage. This finding underscores the importance of high-resolution near-field seismic monitoring for capturing secondary and precursory failure processes that may not be observable through conventional geotechnical investigations.

Ambient-noise cross-correlation analyses reveal measurable post-collapse modifications in Green's functions, particularly within the 0.5–4.0 Hz frequency range. These temporal changes indicate alterations in near-surface elastic properties, likely associated with stiffness reduction and damage accumulation induced by cavity growth and collapse. The observed frequency-dependent sensitivity highlights the effectiveness of high-frequency surface waves for detecting shallow subsurface perturbations, demonstrating that continuous ambient-noise monitoring provides a viable, non-invasive tool for tracking subsurface property changes related to sinkhole development in urban settings.

Overall, this study demonstrates the effectiveness of dense urban seismic networks in characterizing sinkhole failure mechanisms and monitoring subsurface cavity evolution. The integration of seismic waveform analysis, source mechanism interpretation, and ambient-noise interferometry provides a robust framework for resolving both the dynamic collapse process and associated changes in ground properties. Such an approach has significant potential to enhance ground stability assessment and hazard mitigation strategies in densely populated urban

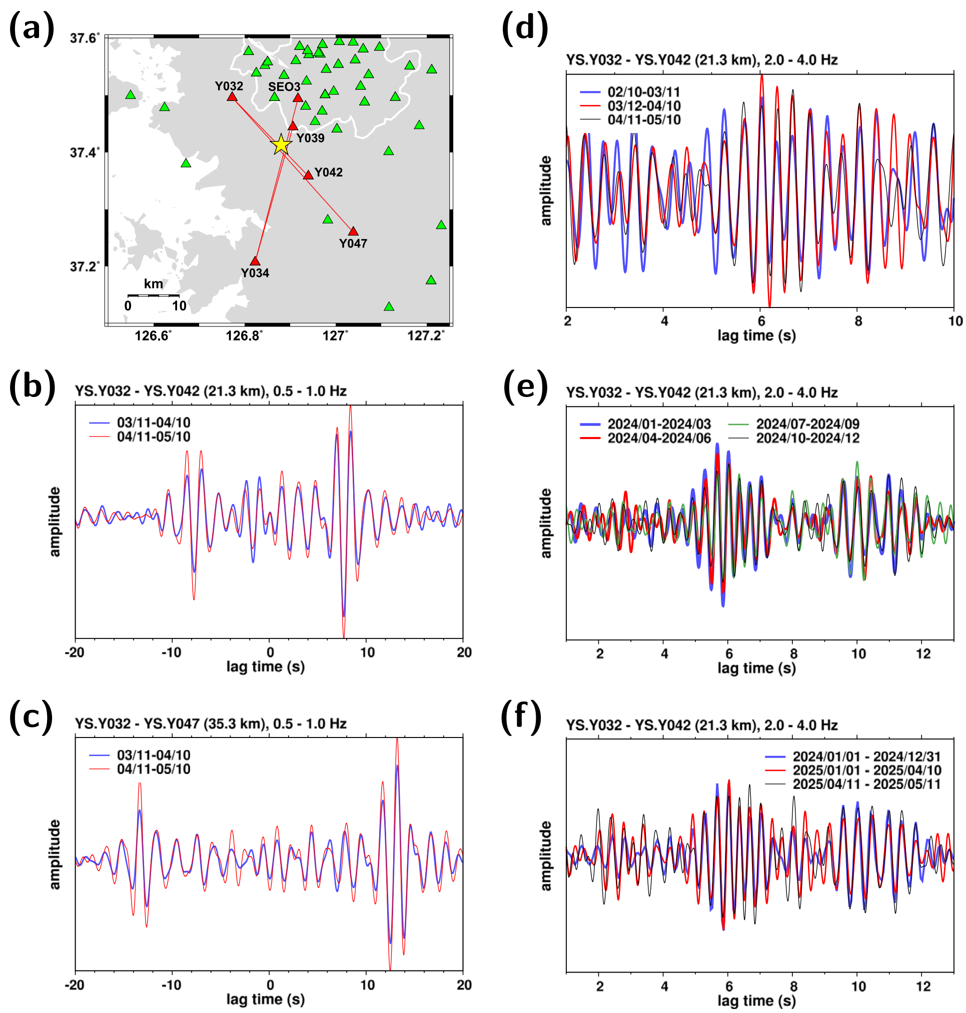

Fig. 11. (a) Map of interstation paths across the sinkhole site, and stacked ambient-noise crosscorrelation functions for interstation paths (b) Y032-Y042 in frequencies of 0.5–1.0 Hz, (c) Y032-Y047 in 0.5–1.0 Hz, (d) Y032-Y042 in 2.0–4.0 Hz, (e) Y032-Y042 in 2.0–4.0 Hz, and (f) Y032-Y042 in 2.0–4.0 Hz. The time periods for crosscorrelation function stacking are indicated. The stacked ambient-noise cross-correlation functions yield wavetrains composed of wavelets traveling between stations. The amplitudes do not have absolute physical values. The Green's functions for the interstation paths are retrieved stably.

areas, where anthropogenic sinkholes pose increasing risks to public safety and critical infrastructure.

The identified two-stage failure mechanism comprising lateral cavity expansion, vertical roof collapse, and distributed brittle damage represents a fundamental process governing anthropogenic sinkhole collapse in urban environments. The results further demonstrate that seismic properties are directly linked to subsurface mechanical degradation, including stiffness reduction and damage accumulation. This linkage provides a transferable framework for incorporating seismic monitoring into ground stability assessment and sinkhole hazard mitigation practices.

CRediT authorship contribution statement

Tae-Kyung Hong: Writing – review & editing, Writing – original draft, Methodology, Investigation, Funding acquisition, Formal analysis. **Byeongwoo Kim:** Investigation, Formal analysis, Data curation. **Seongjun Park:** Investigation, Formal analysis. **Jeongin Lee:** Investigation, Formal analysis. **Junhyung Lee:** Investigation, Formal analysis.

Declaration of competing interest

The authors declare the following financial interests/personal relationships which may be considered as potential competing interests: Tae-Kyung Hong reports financial support was provided by National Research Foundation of Korea. If there are other authors, they declare that they have no known competing financial interests or personal relationships that could have appeared to influence the work reported in this paper.

Acknowledgment

We are grateful to Dr. Hesham El Naggar (editor) and two anonymous reviewers for constructive review comments. The seismic records were collected from Korea Meteorological Administration (KMA) and Korea Institute of Geoscience and Mineral Resources. This work was supported by the Korea Meteorological Administration Research and Development Program under grant KMI2022-00710. Additionally, this research was partly supported by National Research Foundation of Korea (RS-2025-23963785).

Appendix A. Supplementary data

Supplementary material related to this article can be found online at https://doi.org/10.1016/j.soildyn.2026.110522.

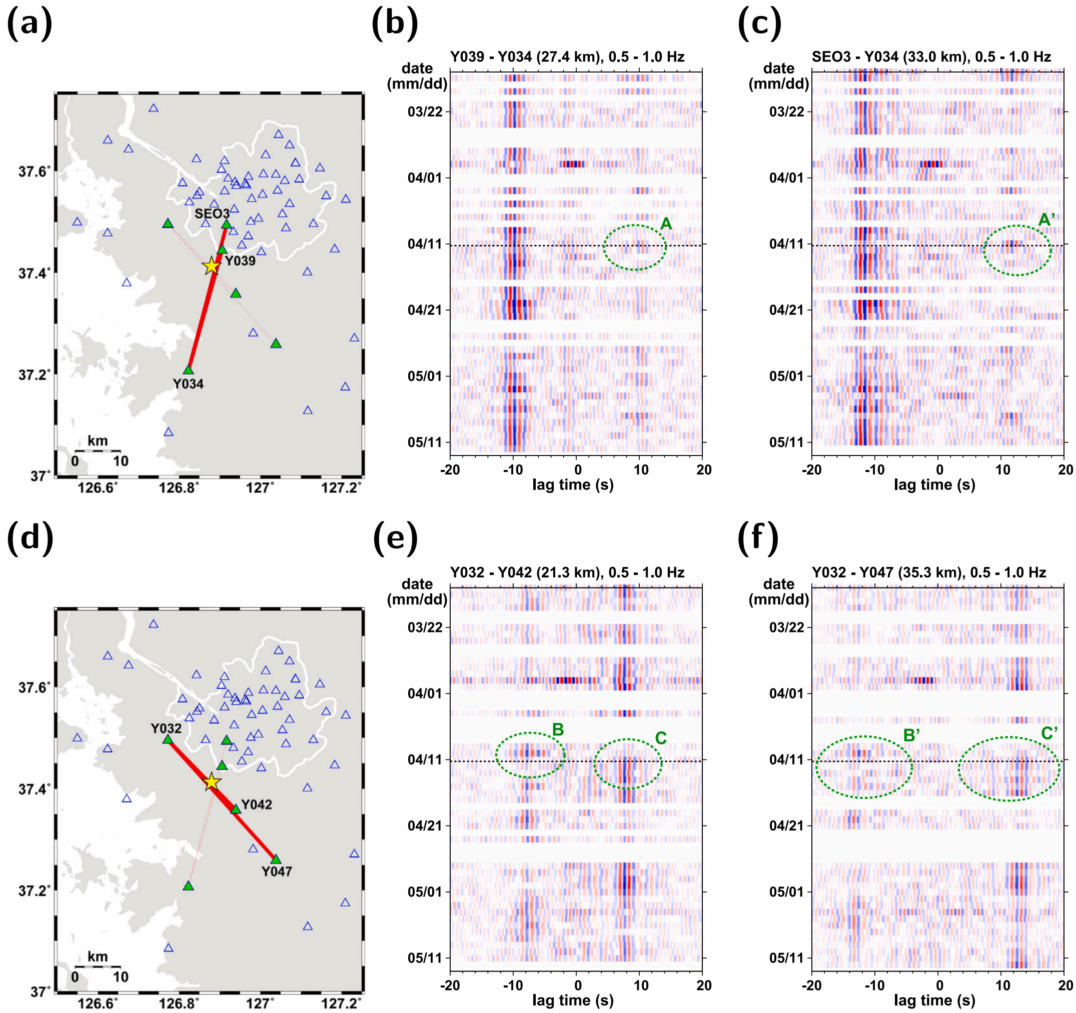

Fig. 12. Daily variation of 1-day-stacked ambient-noise crosscorrelation functions in frequencies of 0.5–1.0 Hz: (a) map of interstation paths in NE-SW, and results for paths (b) Y039-Y034 and (c) SEO3-Y034, and (d) map of interstation paths in NW-SE, and results for paths (e) Y032-Y042, and (f) Y032-Y047. Crosscorrelation functions for one day are stacked. Stable Green's functions are retrieved. The timing of sinkhole event is indicated (dotted line). Apparent discontinuity in daily Green's functions occurs over the sinkhole occurrence date (A, A', B, B', C, C').

Data availability

Data will be made available on request.

References

[1] Strzałkowski P. Sinkhole formation hazard assessment. Environ Earth Sci 2019;78:9. http://dx.doi.org/10.1007/s12665-018-8002-5.

[2] Gutiérrez F, Benito-Calvo A, Carbonel D, Desir G, Sevil J, Guerrero J, Martínez-Fernández A, Karamplaglidis T, García-Arnay A, Fabregat I. Review on sinkhole monitoring and performance of remediation measures by high-precision leveling and terrestrial laser scanner in the salt karst of the ebro valley. Spain Eng Geol 2019;248:283–308. http://dx.doi.org/10.1016/j.enggeo.2018.12.004.

[3] Gutiérrez F. Sinkhole hazards. In: Oxford research encyclopedia of natural hazard science. Oxford: Oxford University Press; 2016, p. 1–92.

[4] Gutiérrez F, Cooper AH, Johnson KS. Identification, prediction, and mitigation of sinkhole hazards in evaporite karst areas. Environ Geol 2008;53(4):1007–22. http://dx.doi.org/10.1007/s00254-007-0728-4.

[5] Land L. Geophysical records of anthropogenic sinkhole formation in the delaware basin region, southeast new Mexico and west texas, USA. Carbonates Evaporites 2013;28:183–90. http://dx.doi.org/10.1007/s13146-013-0126-9.

[6] Xiao H, Kim YJ, Nam BH, Wang D. Investigation of the impacts of local-scale hydrogeologic conditions on sinkhole occurrence in east-central Florida, USA. Environ Earth Sci 2016;75:1274. http://dx.doi.org/10.1007/s12665-016-6086-3.

[7] Xua J, Heb J, Zhang L. Collapse prediction of karst sinkhole via distributed brillouin optical fiber sensor. Measurement 2017;100:68–71.

[8] Ezersky MG, Frumkin A. Identification of sinkhole origin using surface geophysicalmethods, dead sea, Israel. Geomorphology 2020;364:107225. http://dx.doi.org/10.1016/j.geomorph.2020.107225.

[9] Park CB, Miller RD, Xia J. Multichannel analysis of surface waves. Geophysics 1999;64(3):800–8. http://dx.doi.org/10.1190/1.1444590.

[10] Hong T-K. Seismic investigation of the 26 march 2010 sinking of the South Korean naval vessel cheonanham. Bulletin Seismological Society America 2011;101(4):1554–62.

[11] Hong T-K, Lee J, Park S, Yoon HH, Kim W, Shin JS. Seismic detection of strong ground motions by mw5.6 north Korean nuclear explosion. Scientific Reports 2019;9:5124. http://dx.doi.org/10.1038/s41598-019-41627-x.

[12] Hong T-K, Park S, Chung D, Kim B. Inversion of acoustic thunder source spectral model from thunder-induced seismic waves in megacity. Geophys J Int 2023;233(1):107–26. http://dx.doi.org/10.1093/gji/ggac440.

[13] Hong T-K, Lee J, Lee G, Lee J, Park S. Correlation between ambient seismic noises and economic growth. Seismol Res Lett 2020;91(4):2343–54.

[14] Hong T-K, Park S, Lee J. Roles of subway speed and configuration on subway-induced seismic noises in an urban region. J Appl Geophys 2022;202:104668. http://dx.doi.org/10.1016/j.jappgeo.2022.104668.

[15] Kim B, Hong T-K, Lee J, Park S, Lee J. Potential seismic hazard in seoul, South Korea: a comprehensive analysis of geology, seismic and geophysical field observations, historical earthquakes, and strong ground motions. Bull Seismol Soc Am 2024;114(2):982–1002. http://dx.doi.org/10.1785/0120230015.

[16] Lee J, Hong T-K, Park S, Lee J, Chung D, Kim B. Laterally varying crustal and quaternary fault-zone structures in the seoul metropolitan area, South Korea from a joint inversion analysis based on dense seismic arrays. Bull Seismol Soc Am 2022;112(4):1935–59. http://dx.doi.org/10.1785/0120210197.

[17] Dreger DS, Helmberger DV. Broadband modeling of local earthquakes. Bull Seismol Soc Am 1990;80:1162–79.

[18] Herrmann RB. Computer programs in seismology: an evolving tool for instruction and research. Seismol Res Lett 2013;84:1081–8. http://dx.doi.org/10.1785/0220110096.

[19] Zhu L, Ben-Zion Y. Parametrization of general seismic potency and moment tensors for source inversion of seismic waveform data. Geophysical Journal International 2013;194(2):839–43. http://dx.doi.org/10.1093/gji/ggt137.

[20] Zhou R-M, Stump BW. Rayleigh waves generated by mining explosions and upper crustal structure around the powder river basin, wyoming. Bull Seismol Soc Am 2004;94(4):1410–29. http://dx.doi.org/10.1785/012003152.

[21] Kil D, Hong T-K, Chung D, Kim B, Lee J, Park S. Ambient noise tomography of upper crustal structures and quaternary faults in the seoul metropolitan area and its geological implications. Earth Space Science 2021;8:e2021A001983. http://dx.doi.org/10.1029/2021EA001983.

[22] Park S, Hong T-K. Continent-side uplifted mantle and geological imprints along a paleo rift in the western east sea (sea of Japan). Journal Geophysical Research: Solid Earth 2024;129:e2024B029049. http://dx.doi.org/10.1029/2024JB029049.

[23] Kennett BLN. Seismic wave propagation in stratified media. Cambridge: Cambridge University Press; 1983.

[24] Muller G. The reflectivity method: a tutorial. J Geophys 1985;58(1):153–74.

[25] Hong T-K, Lee J, Kim B, Park S, Lee J, Kim DG, Kang T-S. Lower-crustal rupture of the 1952 mw 6.3 suburban pyongyang earthquake: insights into seismogenic reactivation in a paleo-collision zone and seismic hazard potential. Bulletin Seismological Society America 2025;115(6):2640–56. http://dx.doi.org/10.1785/0120250104.

[26] Shapiro NM, Campillo M. Emergence of broadband Rayleigh waves from correlations of the ambient seismic noise. Geophysical Research Letters 2004;31:L07614. http://dx.doi.org/10.1029/2004GL019491.

[27] Yang Y, Ritzwoller MH, Levshin AL, Shapiro NM. Ambient noise Rayleigh wave tomography across Europe. Geophys J Int 2007;168:259–74. http://dx.doi.org/10.1111/j.1365-246X.2006.03203.x.

[28] Yao H, van der Hilst RD. Analysis of ambient noise energy distribution and phase velocity bias in ambient noise tomography, with application to SE tibet. Geophys J Int 2009;179(2):1113–32.

[29] Hanasoge SM. The influence of noise sources on cross-correlation amplitudes. Geophys J Int 2013;192(1):295–309.

[30] Boschi L, Weemstra C. Stationary-phase integrals in the cross correlation of ambient noise. Rev Geophys 2015;53:411–51. http://dx.doi.org/10.1002/2014RG000455.

[31] Ermert L, Villasenor A, Fichtner A. Cross-correlation imaging of ambient noise sources. Geophys J Int 2016;204(1):347–64. http://dx.doi.org/10.1093/gji/ggv460.

[32] Ayala-Garcia D, Curtis A, Branicki M. Seismic interferometry from correlated noise sources. Remote Sens 2021;13(14):2703. http://dx.doi.org/10.3390/rs13142703.

[33] Berteussen KA. Moho depth determinations based on spectral-ratio analysis of NORSAR long-period p waves. Phys Earth Planet Inter 1977;15(1):13–27.

[34] Kennett BL, Engdahl ER, Buland R. Constraints on seismic velocities in the earth from traveltimes. Geophys J Int 1995;122(1):108–24.